

## Supporting Information

### Efficient Diffusion of Superdense Lithium via Atomic Channel for Dendrite-Free Lithium-Metal Batteries

**Authors:** Shiyuan Zhou<sup>+,a</sup>, Weixin Chen<sup>+,a</sup>, Jie Shi<sup>+,b</sup>, Gen Li,<sup>a</sup> Fei Pei,<sup>a</sup> Sangui Liu,<sup>a</sup> Weibin Ye,<sup>d</sup> Liangping Xiao,<sup>a</sup> Ming-Sheng Wang,<sup>d</sup> Dan Wang,<sup>b</sup> Yu Qiao,<sup>a,g</sup> Ling Huang,<sup>a</sup> Gui-Liang Xu,<sup>c</sup> Hong-Gang Liao,<sup>\*,a,g</sup> Jian-Feng Chen,<sup>b</sup> Khalil Amine<sup>c,e,f</sup> and Shi-Gang Sun<sup>a</sup>

#### Affiliations:

*a* State Key Laboratory of Physical Chemistry of Solid Surfaces, Collaborative Innovation Center of Chemistry for Energy Materials, College of Chemistry and Chemical Engineering, Xiamen University, Xiamen 361005, P. R. China. E-mail: [hgliao@xmu.edu.cn](mailto:hgliao@xmu.edu.cn) (*H. Liao*)

*b* State Key Laboratory of Organic Inorganic Composites, Beijing University of Chemical Technology, Beijing 100029, P. R. China.

*c* Chemical Sciences and Engineering Division, Argonne National Laboratory, 9700 South Cass Avenue, Lemont, IL 60439, USA

*d* State Key Laboratory of Physical Chemistry of Solid Surfaces, College of Materials, Pen-Tung Sah Institute of Micro-Nano Science and Technology, Xiamen University, Xiamen 361005, P. R. China.

*e* Materials Science and Engineering, Stanford University, Stanford, CA, USA

*f* Institute for Research & Medical Consultations, Imam Abdulrahman Bin Faisal University (IAU), Dammam, Saudi Arabia

*g* Innovation Laboratory for Sciences and Technologies of Energy Materials of Fujian Province (IKKEM), Xiamen 361005, P. R. China.

+ These authors contributed equally to this work.

\*Correspondence to: [hgliao@xmu.edu.cn](mailto:hgliao@xmu.edu.cn)

## Table of Contents

### 1. Experimental Procedures

1.1 Fabrication of Bulk Diffusion Li Conductor (BDLC) and Graphite Carbon (GC)

1.2 Material Characterization

1.3 In-Situ Transmission Electron Microscopy (TEM) Observation

1.4 Electrochemical Measurements

1.5 SEM and TEM Investigation of Cycled Electrode Materials

1.6 Molten Li Adsorption for the Preparation of Li@BDLC

1.7 Computational Models and Methods

1.8 Estimation of the Ratio between C and Li

1.9 Discussion of the Reciprocal Lattice Rod

### 2. Supplementary Characterization Result Figures S1-S30

### 3. Supplementary Tables S1-S4

### 4. Supplementary Videos S1-S5

### 5. References

## Section 1. Experimental Procedures

### 1.1 Fabrication of BDLC and GC

Consisting of highly crystallized graphite layers, commercial carbon paper has been considered as a competitive anode due to its higher surface area, flexible structure and light weight. A molecular tunnelling strategy was introduced for the preparation of BDLC with abundant atomic channels based on the carbon paper (Toray Industry). Specifically, the carbon paper was rinsed with ethanol and deionized water for several times, and dried under vacuum at 60 °C overnight before use. Then it was transferred into the tube furnace and heated at 450 °C under ammonia/argon atmosphere (9:1 by volume). Based on the penetration of thermal-activated NH<sub>3</sub> free radicals at the specific environmental condition, BDLC was obtained with widened graphite layers channels, abundant intralayer voids and N active sites. For the control experiment, the pristine carbon paper with standard graphite layers was labeled as GC (graphite carbon).

### 1.2 Material Characterization

The morphology and element distribution of BDLC, GC were characterized by field emission scanning electron microscope (SEM, ZEISS, Germany), TEM, aberration-corrected TEM and energy dispersive X-ray spectroscopy (FEI Tecnai 20, USA and FEI Themis, USA). The chemical environment and bonding information were detected by X-ray photoelectron spectroscopy (XPS, PHOIBOS150, Germany). Raman spectroscopy (LabRam HR, France) was used at 532 nm wavelength.

### 1.3 In-Situ TEM Observation

The in-situ TEM electrochemical experiment was carried out on FEI Tecnai 20 at an acceleration voltage of 200 kV. The TEM-STM in-situ sample holders (ZepTools Technology and Chip-Nova Co. Ltd., China) were used to demonstrate the plating/stripping process of BDLC and GC. A copper wire attached with BDLC/GC nanosheets was employed as working electrode and a tungsten wire covered with Li was regarded as the counter electrode. A thin Li<sub>2</sub>O layer on the surface of Li was acted as the all-solid-state electrolyte for Li-ion diffusion. A relative bias of -3 V/3 V was induced between two electrodes during the plating/stripping process.

### 1.4 Electrochemical Measurements

The electrochemical performance was conducted in the coin-type cells (CR2032). For the half-cell tests, BDLC and GC (16 mm in diameter) were assembled with Li anodes (500 μm in thickness), electrolyte and polypropylene separators (Celgard 2500) in an argon-filled glovebox. The used electrolyte was 1 M LiPF<sub>6</sub> in ethyl methyl carbonate/ethylene carbonate mixture (1:1 by volume) with 5 wt.% of fluoroethylene carbonate as an additive. 70 μL of electrolyte was used in each cell. After a pre-cycle at 0.2 mA cm<sup>-2</sup> between 0 and 1.0 V for 5 cycles (for the formation of a stable SEI layer), galvanostatic cycling was conducted with a stripping potential cutoff of 1.0 V, including 1 mA cm<sup>-2</sup> for 2 mAh cm<sup>-2</sup> (Figure 5a), 2, 5 and 8 mA cm<sup>-2</sup> for 1 mAh cm<sup>-2</sup> (Figure 5b), 0.5 mA cm<sup>-2</sup> for 5 mAh cm<sup>-2</sup> (Figure S21). For the symmetric-cell tests, BDLC and GC were assembled in half cells for electrodeposition of Li. After a pre-cycle at 0.2 mA cm<sup>-2</sup> between 0 and 1.0 V for 5 cycles, 3 mAh cm<sup>-2</sup> of Li was electrodeposited at 0.2 mA cm<sup>-2</sup> to obtain Li@BDLC, Li@GC, Li@Cu, and then the two identical electrodes were re-assembled in coin-type cells cycling at 1 and 3 mA cm<sup>-2</sup> for 1 mAh cm<sup>-2</sup>. For the full-cell tests, the pre-electrodeposited Li@BDLC and Li@GC were assembled with LiFePO<sub>4</sub> (LFP, Gotion High-Tech; 12 mm

in diameter, LFP:acetylene black:PVDF 93:4:3 mass ratio) cathode. The LFP cathode was calendared by a built-in roll press before battery assembly. The areal mass loading of LFP was controlled at 25, 20 and 10 mg cm<sup>-2</sup> (12 mm in diameter), coupled with 2.5, 2.5 and 1.2 mA h cm<sup>-2</sup> of Li@BDLC (0.2 mA cm<sup>-2</sup> for pre-electrodeposition, 16 mm in diameter), respectively. The batteries are activated between 2.5 and 4.0 V (0.05 C for rate performance, 0.2 C for cycling performance). To further evaluate the practical application prospects, BDLC was directly used as interlayer between 100 μm Li foil and separator in LFP full cells. The frequency range of the electrochemical impedance spectroscopy (EIS) tests was from 100 kHz to 10 mHz. The electrochemistry tests were carried out on LAND cell test instrument (CT2001A) and Multi Autolab electrochemical workstation (M204, Netherlands). All electrochemical tests were carried out at room temperature.

### 1.5 SEM and TEM Investigation of Cycled Electrode Materials

The cycled coin-type cells were disassembled in an argon-filled glovebox and the electrodes were rinsed with DME thoroughly to remove residual electrolytes. The dried electrodes were sealed in air-isolated container in glovebox and transferred into the SEM equipment to avoid air exposure. The morphologies of cycled Li@BDLC and Li@GC were characterized by SEM (SU4800). The samples for TEM study were also prepared in an argon-filled glovebox and was investigated by a FEI Talos at 200 kV.

### 1.6 Molten Li Adsorption for the Preparation of Li@BDLC

The molten Li adsorption was carried out in an argon-filled glovebox. In a typical process, BDLC (16 mm in diameter) was placed on the top of molten Li made by heating fresh Li foil on a hotplate to 330 °C. Subsequently, benefitted from its lithium-philicity, BDLC was easy to be wetted and filled by the molten Li in a short time to form the Li@BDLC composite. The mass loading of Li in Li@BDLC could be controlled by adjusting the adsorption time.

### 1.7 Computational Models and Methods

The graphene model was selected to simplify the calculation for the graphitized model with C active sites or N active sites or no active sites in this work. As Supplementary Fig. S4 and S5 shown, the unit cell of 17.09 Å×17.22 Å×17 Å was chosen and it contained 112 C atoms initially. Active sites of a single C atom or two C atoms or three C atoms were constructed in the models with C active sites or N active sites. It was worth noted that the C atoms around the active sites were substituted by N atoms in BDLC models.

Spin-unrestricted density functional theory (DFT) calculations for analyses of the interaction between Li and carbon materials and the interlayer transportation of Li were carried out by using Vienna Ab initio Simulation Package (VASP.5.4.4)<sup>1</sup>. The correlation energy and exchange energy were calculated by using the Perdew-Burke-Ernzerhof (PBE) functional of the generalized gradient approximation (GGA)<sup>2</sup>. The wave function projected in the real space was expanded by the plane wave whose cutoff energy was 400 eV. Brillouin zone sampling was restricted to the  $\Gamma$  point in structural optimizations and 3×3×1 k-point for electronic property calculations particularly. During the structural optimizations, all atoms were allowed to fully relax until the maximum force on them was less than 0.01 eV/Å. The binding energy of Li was given by:

$$E_{binding} = E_{total} - E_{substrate} - E_{Li} \text{ (Supplementary Eq. S1)}$$

where the  $E_{total}$  is the energy of the complex including the graphene substrate and adsorbed Li atom,  $E_{substrate}$  is the total energy of the graphene sheet with C active sites or N active sites or no active sites, and  $E_{Li}$  is the energy of the isolated Li atom.

The annealing method of ab-initio molecular dynamics (AIMD) simulations were used to explore the diffusion of high-density Li between the layers in BDLC and graphite layers. We chose a double-layer graphene model with 96 C atoms in single layer (4 C atoms in each layer in BDLC were replaced by graphitic N atoms). The timestep was set as 2 fs, and the temperature was increased to 300 K at a heating rate of 0.1 K/fs. Average the atomic z coordinates in the graphene layer during the AIMD operations to obtain the real-time interlayer distances. The final annealing structures were fully optimized to get the average interlayer spacings in Fig. 2a and Fig. S1b.

The climbing image nudged elastic band (CI-NEB)<sup>3</sup> method was employed to search for the transition states and minimum energy paths (MEP) for the diffusion of Li in BDLC and graphite layers. The models about different active sites were set as the structures in Supplementary Fig. S8 and S9, with a triple-atom active site (i.e. pyrrolic-N sites in the BDLC model) and a large void. The models about different layer spacings were shown in Supplementary Fig. S3, in which the distance between two graphene sheets was 3.4 Å (graphite layer model) and 6.8 Å (BDLC model), respectively. There was no vacuum layer above the graphene sheets, which was used to describe the Li diffusion in the bulk materials. Li atom diffused from the large void to the triple-atom active site (or from one side of the two graphitic sheets to an interlayer position of the two graphitic sheets) to complete an interlayer diffusion process. The models of Li stripping from BDLC were shown in Fig. 4e, in which the distances between two graphene sheets were both 6.8 Å. Since in-situ TEM plating/stripping would lead to the SEI layers mainly composed of Li<sub>2</sub>O layers, which was consequently considered for surface Li stripping. A single layer of Li<sub>2</sub>O was fixed on the graphite sheets at an optimal distance (~ 2.1 Å) to imitate the surface deposition at the beginning of the charging process. A vacuum layer of 12 Å was set and the lattice length in the y direction is 14.37 Å (with a mismatch about 2.5 %). As shown in the potential energy profile, the symmetry of surface structure controlled the migration process of Li over Li<sub>2</sub>O, as the potential energy was equal before and after migration. Therefore, we could infer that the long-distance migration barrier on the surface was equivalent to its short-range migration barrier. The spring force between adjacent images was set to 5.0 eV/Å and the exact location of the saddle point was finally approached until the forces on each atom were less than 0.02 eV/Å. The energy barrier was calculated by:

$$E_{barrier} = E_{TS} - E_{initial} \text{ (Supplementary Eq. S2)}$$

where the  $E_{TS}$  is the energy of the transition state and  $E_{initial}$  is the energy of initial state. In order to accurately describe the dispersion interaction, all calculations performed by VASP used the semiempirical van der Waals correction method of Grimme (DFT-D3).<sup>4</sup>

The model for studying the intralayer diffusion of Li consisted of 96 Li atoms above and 4 graphene layers below, as shown in Fig. 2e and Supplementary Fig. S11. The hybrid Gaussian and plane waves method as implemented in the Quickstep module of the CP2K package<sup>5</sup> was employed for AIMD simulations. The PBE functional with the Grimme van der Waals correction method was used to calculate the Li diffusion. The GTH pseudopotentials combined with DZVP-MOLOPT-SR-GTH basis set was utilized for all atoms.<sup>6</sup> The time step was set as 2 fs, and the simulations were carried out in 700 K NVT ensemble. To compare the difference of Li intralayer diffusion in BDLC and graphite layers, we calculated the mean squared displacement along the z-direction ( $MSD-Z$ ). That is,

$$MSD-Z = \langle (z - z_0)^2 \rangle = \frac{1}{N} \sum_{n=1}^N (z_n(t) - z_n(0))^2 \quad (\text{Supplementary Eq. S3})$$

where  $N$  is the number of Li atoms,  $z_n(t)$  is the reference z position of each Li atom,  $z_n(0)$  is the z position of each Li atom at time  $t$ .

### 1.8 Estimation of the Ratio between C and Li

The contrasts of TEM image were mainly composed of diffraction contrast, mass-thickness contrast and phase contrast. For the in-situ TEM imaging in this experiment (Supplementary Fig. S17 and Video S1), the mass-thickness contrast, contributed by the scattering of C and Li atoms, was the dominant factor. The intensity in images were approximately proportional to the average local atomic number.  $N$ ,  $N_{bkg}$ ,  $N_{Li}$ , and  $N_{carbon}$  could be converted into corresponding gray value. In our case, the gray value could be calculated by:

$$V = V_{bkg} - V_{Li} - V_{carbon} \quad (\text{Supplementary Eq. S4})$$

where  $V_{bkg}$ ,  $V_{Li}$ , and  $V_{carbon}$  represent the gray value of background (bkg), Li, and C respectively.  $V$  represents the gray value measured via image J.

As shown in Supplementary Fig. S17c,  $V_{bkg}$  was 139.22. Because Li was fully stripped in Supplementary Fig. S17b,  $V_{Li}$  was 0,  $V_{carbon}$  in Area II was 14.89.

The  $V_{bkg}$  and  $V_{carbon}$  barely changed since the mass and thickness of carbon and bkg remained almost the same during plating/stripping. Then  $V_{Li}$  in Area II under different stripping stage could be calculated:

$$V_{Li} = 124.33 - V \quad (\text{Supplementary Eq. S5})$$

From Supplementary Fig. S17d, we deduced that  $V_{Li}$  was 22.17.

The ratio of gray value in Supplementary Fig. S17f could be calculated by dividing the  $V_{Li}$  by  $V_{carbon}$ . The ratio of gray value decreased to  $\sim 0$  after stripping, indicating that almost no Li was resided in/on the BDLC.

As reported in previous work,  $\lambda_{Li}$  and  $\lambda_{carbon}$  were 11.3 and 6.0 Å respectively.<sup>7</sup> Therefore, in Area II, it could be deduced that  $L_{Li}$  and  $L_{carbon}$  were 250.5 and 89.3 Å, respectively (Supplementary Eq. S5 and S6), and the overall atomic ratio of Li/C could be estimated by the following equation:

$$\text{overall atomic ratio} = \frac{L_{Li}}{L_{carbon}} \quad (\text{Supplementary Eq. S6})$$

Consequently, the overall atomic ratio reached 2.80.

Besides,  $L_{Li}$  in Supplementary Eq. S5 consisted of  $L_{bulk Li}$  and  $L_{surface Li}$ . The bulk Li and surface Li distribution was measured in Supplementary Fig. S18a. The average thickness of surface-deposited Li ( $L_{surface Li}$ ) was measured to be 95.2 Å after full plating. Considering the imaging mode of transmission electrons, an ideal deposition of Li on both sides (Supplementary Fig. S18b) was investigated. Therefore,  $L_{bulk Li}$  was measured to be 60.1 Å. The atomic ratio of Li/C within bulk could be further estimated by the following equation:

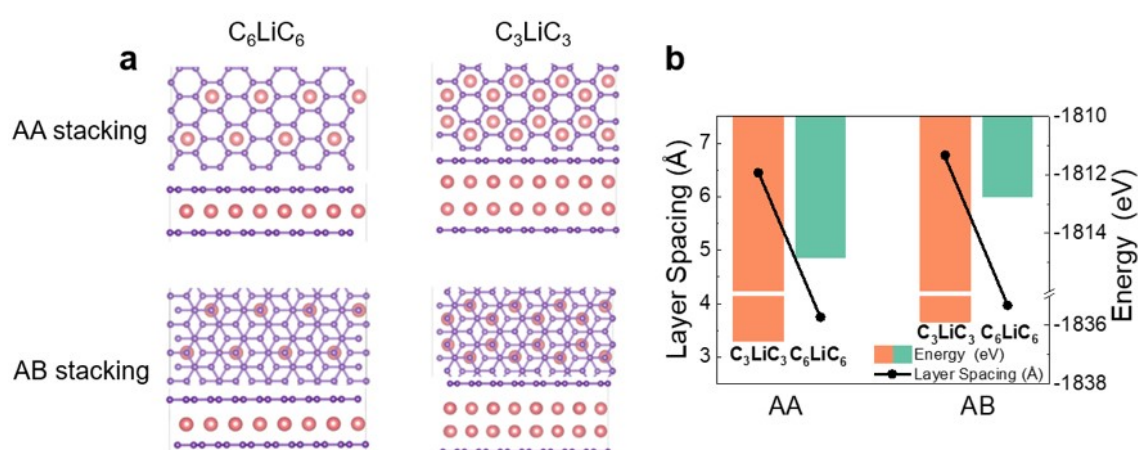
$$atomic\ ratio = \frac{L_{bulk\ Li}}{L_{carbon}} \text{ (Supplementary Eq. S7)}$$

Hence, in Area II (Supplementary Fig. S17), the atomic ratio reached 0.67. Similarly, the atomic ratio of Area III reached 0.27. All the above results were much higher than 0.167 of conventional  $C_6LiC_6$  structure, confirming the superdense Li in the atomic channels of BDLC.

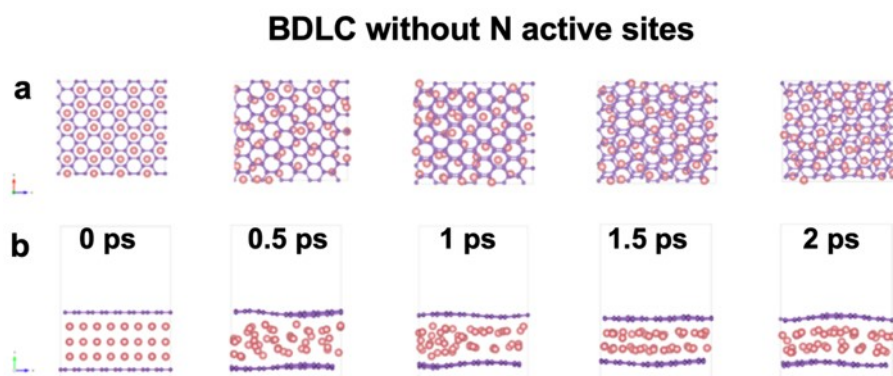
### 1.9 Discussion of the Reciprocal Lattice Rod

The shape effect of the specimen would cause the electron diffraction to deviate from the Bragg condition ( $2d\sin\theta=n\lambda$ ). Due to the difference in crystal structure of specimen, there are various degrees of expansion and deformation inside the crystal, which would lead to the reciprocal lattice to have a certain volume and shape in space. When performing electron diffraction to the thin crystal, the intensity distribution of the diffracted beam has a certain width range, that is, under the condition of slightly deviating from the Bragg condition, there is still a certain intensity of the diffraction beam. Therefore, the reciprocal lattice is no longer a geometric point, but a reciprocal lattice rod that expands along the thickness of the crystal. And the length of reciprocal lattice is inversely proportional to the thickness of crystal, that is, the thinner the crystal, the longer the reciprocal lattice rod.

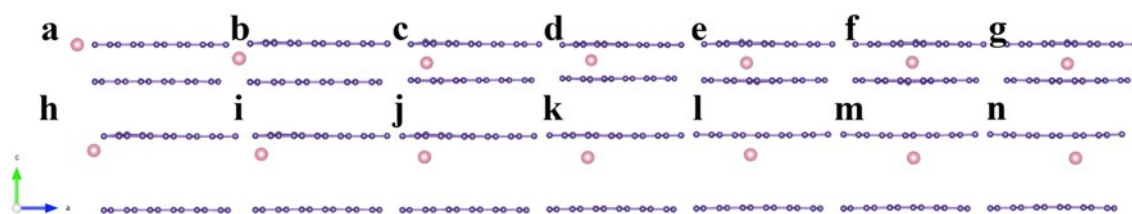
## Section 2: Supplementary Characterization Result Figures S1-S30



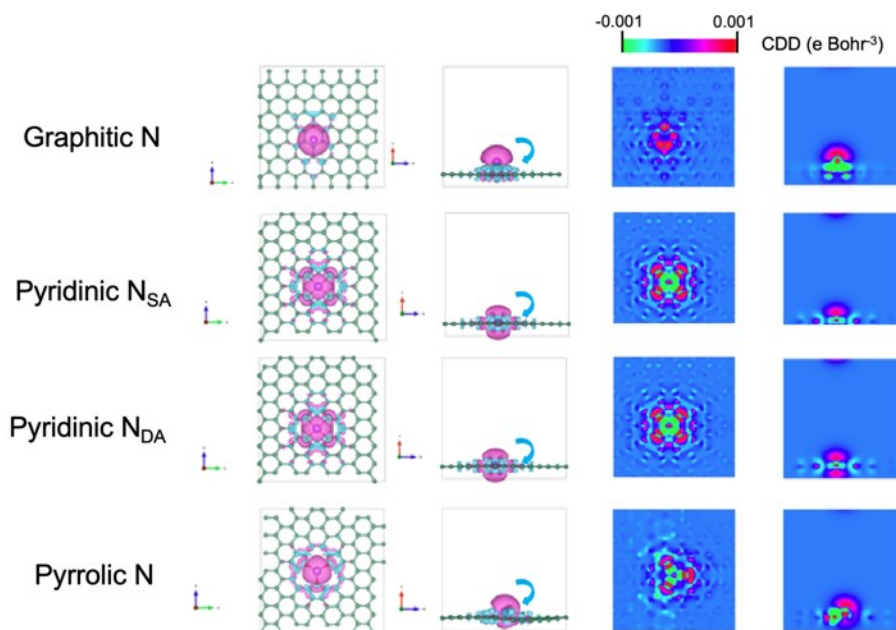
**Supplementary Fig. S1** | (a) Top views and side views of  $C_6LiC_6$  and  $C_3LiC_3$  under AA stacking and AB stacking. (b) Layer spacings and energies of  $C_6LiC_6$  and  $C_3LiC_3$  under AA stacking and AB stacking. The stacking structures of  $C_6LiC_6$  and  $C_3LiC_3$  can maintain six-fold symmetry and the energy differences in (b) reveals that the AA stacking tends to be more stable than the AB stacking. From the perspective of the layer spacing, the structures with AA stacking have a smaller layer spacing and a tighter stacking. The pink and purple balls represent Li and C atoms, respectively.



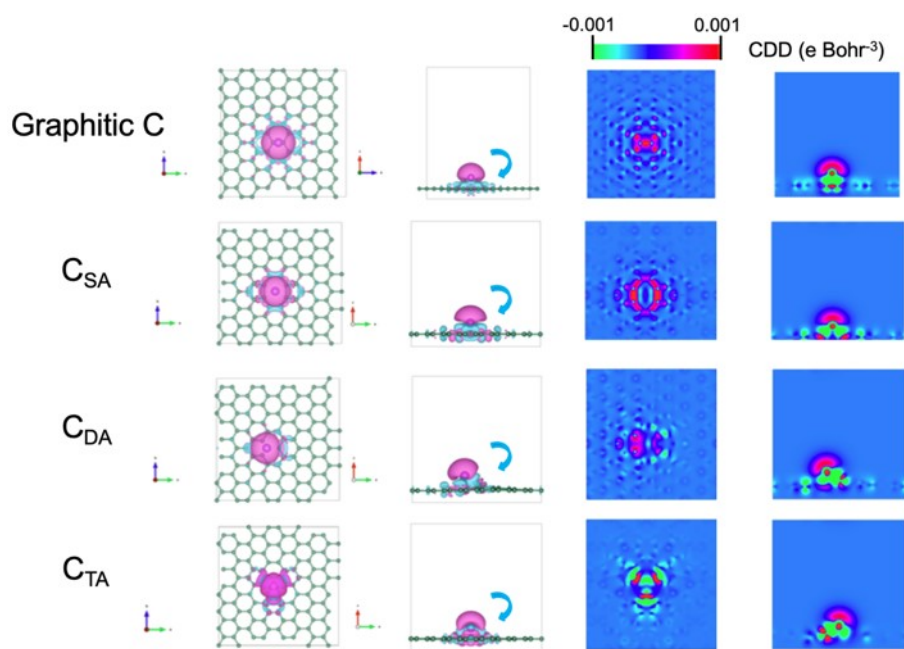
**Supplementary Fig. S2** | Corresponding to Fig. 2a-b in the main text, (a) top views, (b) side views of the AIMD snapshots for interlayer diffusion within BDLC (without N active sites). The pink and purple balls represent Li and C atoms, respectively.



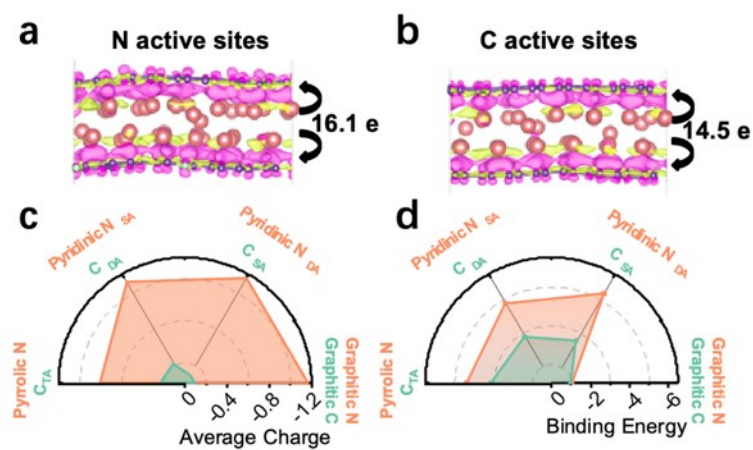
**Supplementary Fig. S3** | Corresponding to Fig. 2d in the main text, (a)-(g) side views of the successive states of Li diffusion within graphite layers (3.4 Å) and (h)-(n) side views of the successive states of Li diffusion within BDLC (6.8 Å). Amongst them, (a) and (i) correspond to the initial state. (f) and (m) correspond to the transition state. (g) and (n) correspond to the final state. The pink and purple balls represent Li and C atoms, respectively.



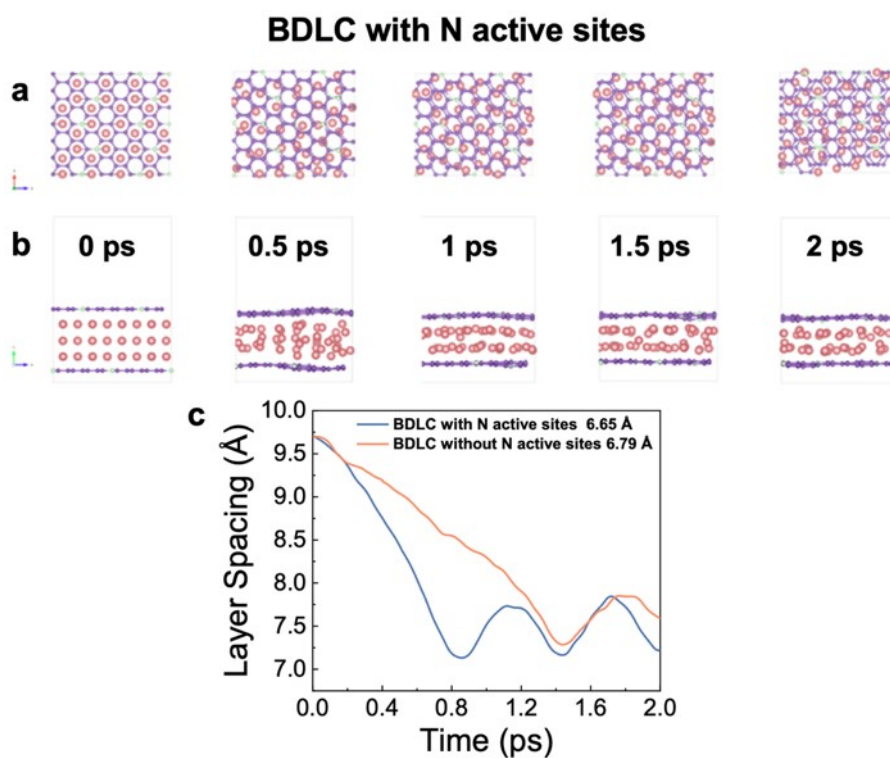
**Supplementary Fig. S4** | Top views and side views of the charge density difference (CDD) and the corresponding CDD slices of graphitic N, single-atom pyridinic N (pyridinic N<sub>SA</sub>), double-atom pyridinic N (pyridinic N<sub>DA</sub>), and pyrrolic N. The green, red, and purple balls represent C, N and Li atoms, respectively. It should be noted that: (i) the graphitic N model was a graphene sheet with no atomic active sites, in which a graphitic C atom was replaced by a N atom, and the adsorbed Li was above the doped-N site; (ii) the pyridinic N<sub>SA/DA</sub> model was a graphene sheet with a single-atom active sites or a double-atom active sites, in which the surrounding graphitic C atoms were all replaced by N atoms, and the adsorbed Li was on the center of the active site; (iii) the pyrrolic N model was a graphene sheet with a penta-atom active site, in which the three C atoms in the three surrounding five-membered rings were all replaced by N atoms, and the adsorbed Li was on the center of the active site.



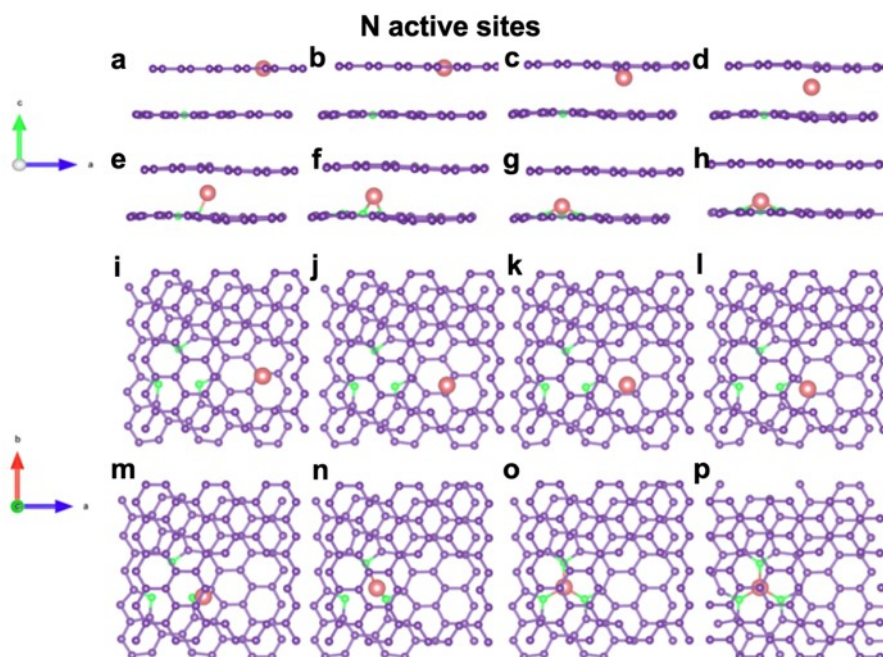
**Supplementary Fig. S5** | Top views and side views of the CDD and the slice of corresponding CDD of graphitic C, single-atom C active site ( $C_{SA}$ ), double-atom C active site ( $C_{DA}$ ), and triple-atom C active site ( $C_{TA}$ ). The green and purple balls represent C and Li atoms, respectively. The models are similar to those in Supplementary Fig. S4, except that there are no substitutions of N atoms.



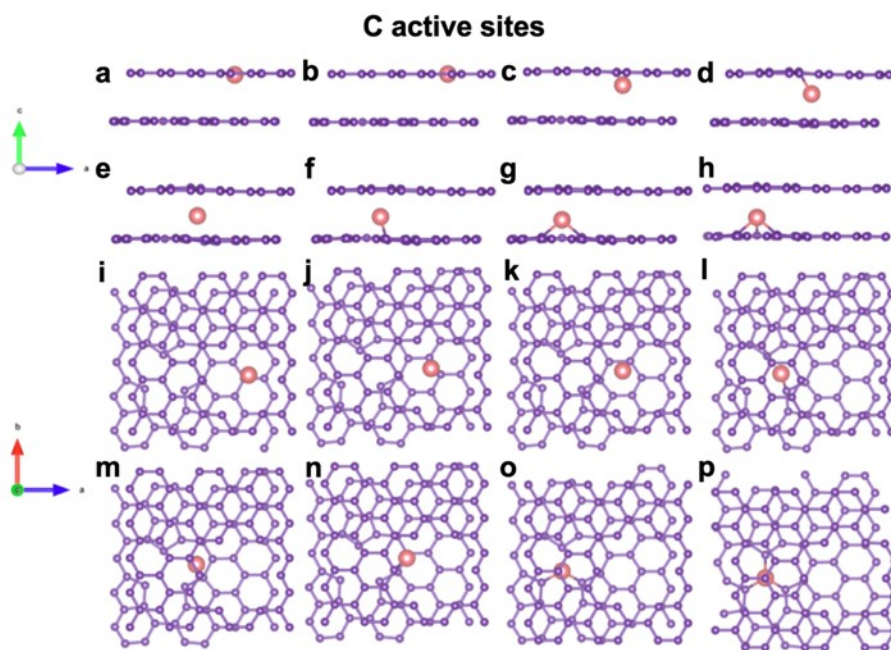
**Supplementary Fig. S6** | CDD of Li in N active sites (a) and C active sites (b). (c) Average charges of the C/N atoms around the active sites and (d) binding energies of Li in different active sites corresponding to the models of Supplementary Fig. S4 and S5. As shown in CDD results (a) and (b), N active sites present a stronger ionization and higher affinity to Li.



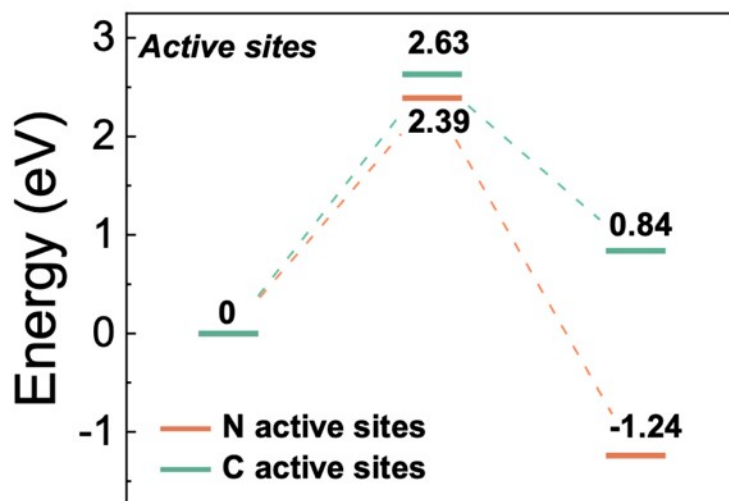
**Supplementary Fig. S7** | (a) top views, (b) side views of the AIMD snapshots for interlayer diffusion within BDLC (with N active sites). (c) Variation of layer spacing over time for interlayer diffusion according to AIMD simulations, regarding BDLC with/without N active sites. Compared with the structures in Supplementary Fig. S2, the interlayer diffusion of Li is accelerated in BDLC with N active sites, which is mainly due to its better lithium-philicity. Especially for the structures at 0.5 and 1 ps, Li in BDLC with N active sites redistributes quickly from a three-layer metastable structure to a two-layer stable structure. The pink, purple and green balls represent Li, C and N atoms, respectively.



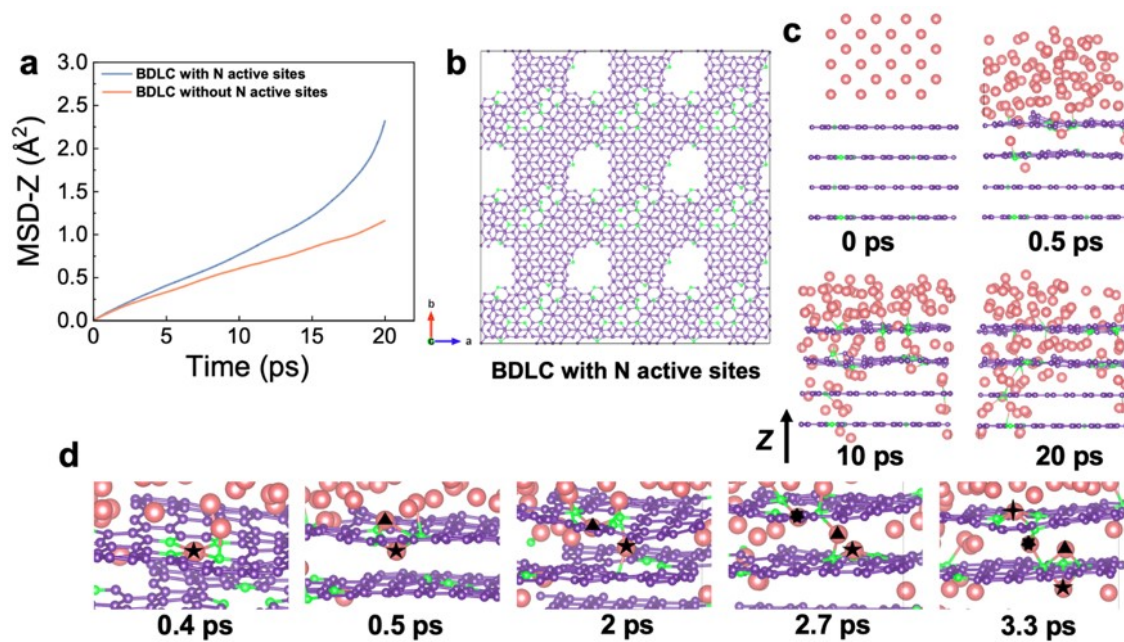
**Supplementary Fig. S8** | (a)-(h) side views of the successive states of the Li interlayer diffusion in N active sites (with a triple-atom N active site and a large void) and (i)-(p) top views of the successive states of the Li interlayer diffusion in N active sites. Amongst them, (a) and (i) correspond to the initial state. (d) and (l) correspond to the transition state. (h) and (p) correspond to the final state. The pink, purple, and green balls represent Li, C and N atoms, respectively.



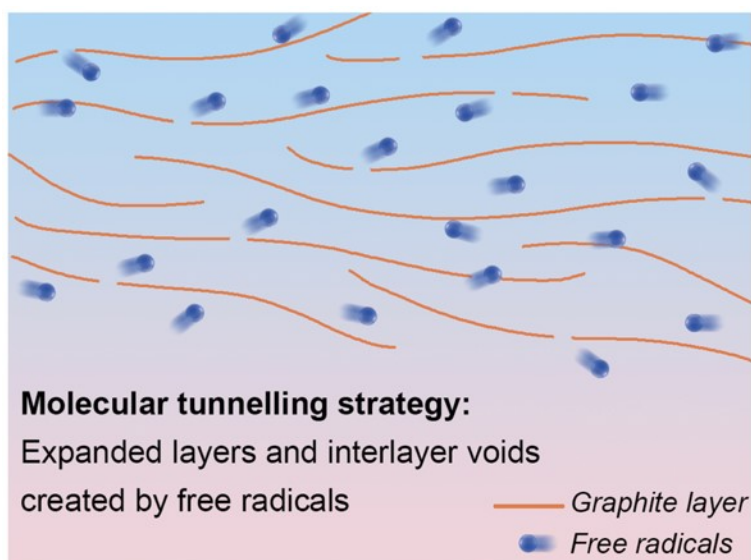
**Supplementary Fig. S9** | (a)-(h) side views of the successive states of the Li interlayer diffusion in C active sites (with a triple-atom C active site and a large void) and (i)-(p) top views of the successive states of the Li interlayer diffusion in C active sites. Amongst them, (a) and (i) correspond to the initial state. (d) and (l) correspond to the transition state. (h) and (p) correspond to the final state. The pink and purple balls represent Li and C atoms, respectively.



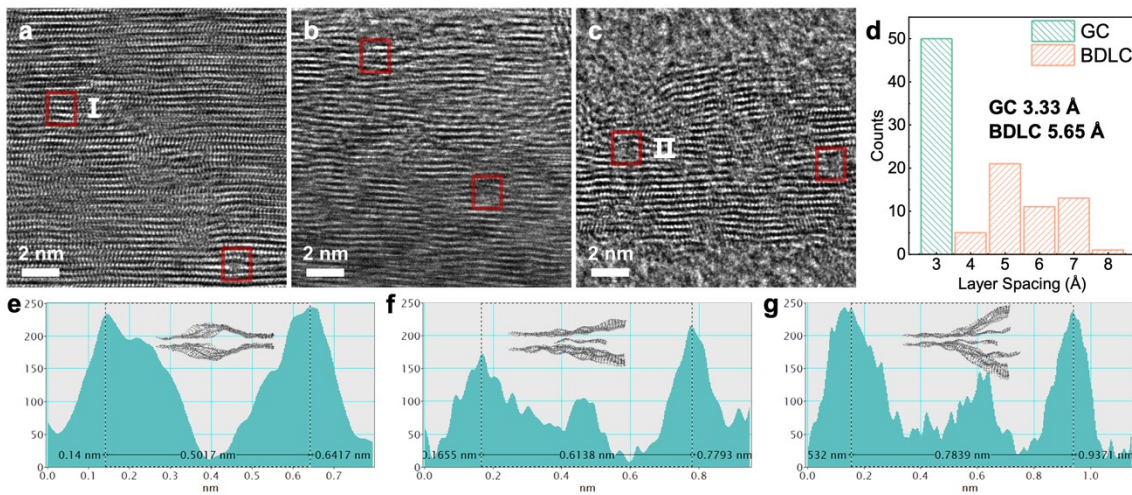
**Supplementary Fig. S10** | Corresponding to Supplementary Fig. S8 and S9, migration energy profiles of Li diffusion regarding different active sites (N and C) at the initial, transition and final state. It should be noted that the response of N active sites to Li migration can lead to a decreased energy barrier and a lower final-state energy, compared with the C active sites.



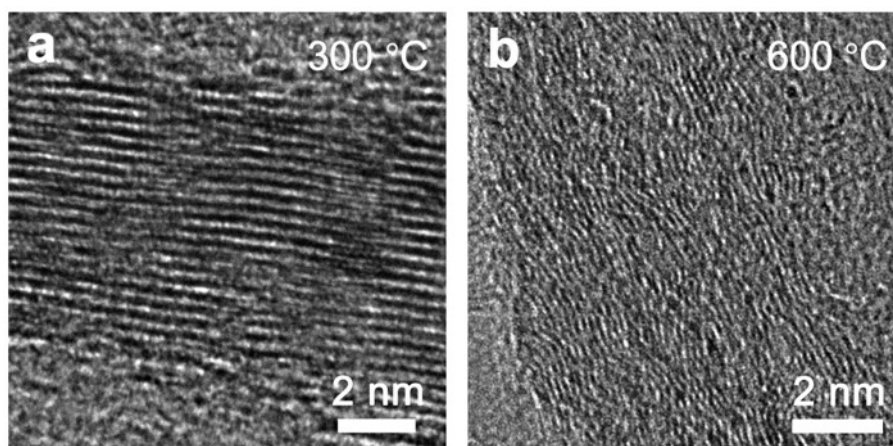
**Supplementary Fig. S11** | (a) MSD curves of Li diffusion along z-axis direction, regarding BDLC with/without N active sites. (b) top view of the constructed model for Li intralayer diffusion simulation within BDLC (with N active sites). (c) and (d) snapshots of AIMD simulations of the cross-layer diffusion through atomic channels. It is worth mentioning that Li could hardly diffuse across the pristine graphite layers if the voids and N active sites are absent according to our calculation. This result highlights the significance of the intralayer atomic channels. As shown in the snapshots (d), N active sites can provide an additional intralayer channel for Li diffusion, as the four Li atoms pass the same N active sites successively.



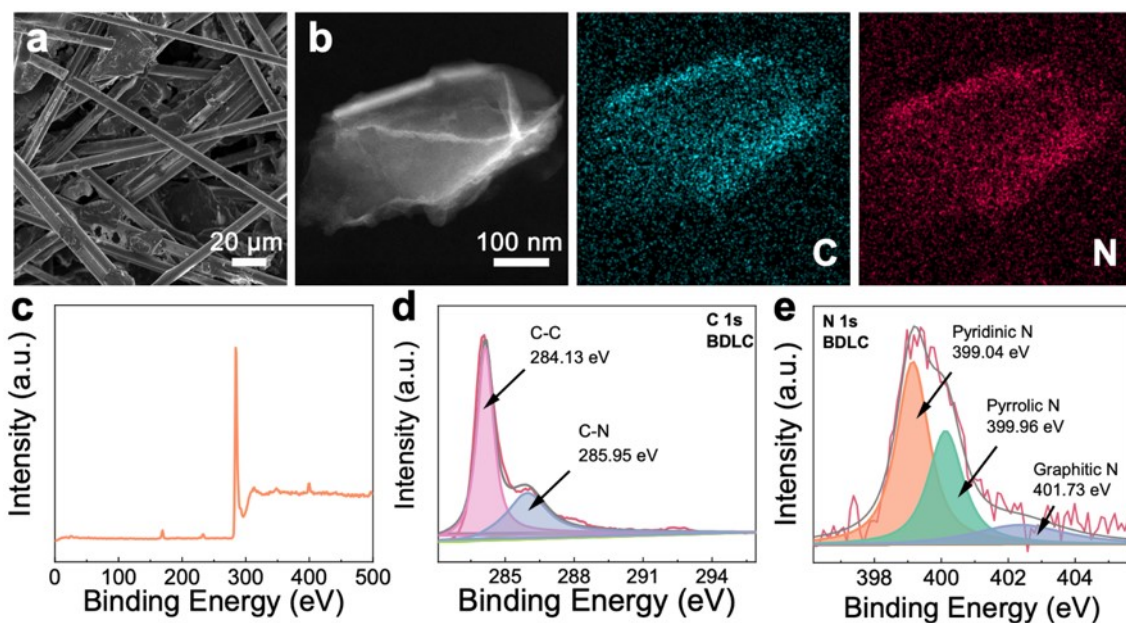
**Supplementary Fig. S12** | Schematic illustration of molecular tunnelling strategy. The  $\text{NH}_3$  decomposes to free radicals such as  $\text{NH}_2$ ,  $\text{NH}$ , and  $\text{H}$  under heating, and the free radicals penetrate and diffuse in the graphite layers, leaving channels with widened layer spacing and intralayer voids simultaneously.<sup>8</sup> This simple method of  $\text{NH}_3$ -based thermal treatment is also easy to scale up and achieve large-scale fabrication, for example, by designing the mechanical components of the tube furnace to have a specific size, and a higher accuracy of temperature rise and control; regulating  $\text{NH}_3$  environment with uniform concentration and flow rate, etc.



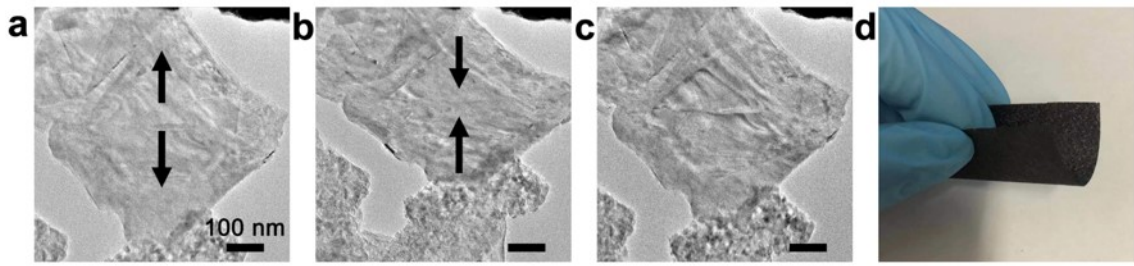
**Supplementary Fig. S13** | (a)-(c) Aberration corrected HRTEM images of BDLC. The typical expanded layer spacings are marked with red squares. (d) Statistics of the layer spacing distribution of BDLC and GC. Profile plots of the calibration for measuring the layer spacings of (e) bulging channel, (f) single-layer-graphene supported channel and (g) multi-layer-graphene supported channel, corresponding to Fig. 3f. It should be noted that the molecular tunnelling would often leave small graphene nanosheets in the undulating interlayer structure, as reflected by the fluctuated intensity in profile plots. Besides, for a typical interlayer structure (I), the layer spacings are expanded to around 4 Å. In some areas (II), the interlayer structure would be further opened, resulting in an expanded interlayer spacing to more than 10 Å. We think this is also beneficial to the diffusion of Li in BDLC, but these large interlayer spacings are not counted in the statistics.



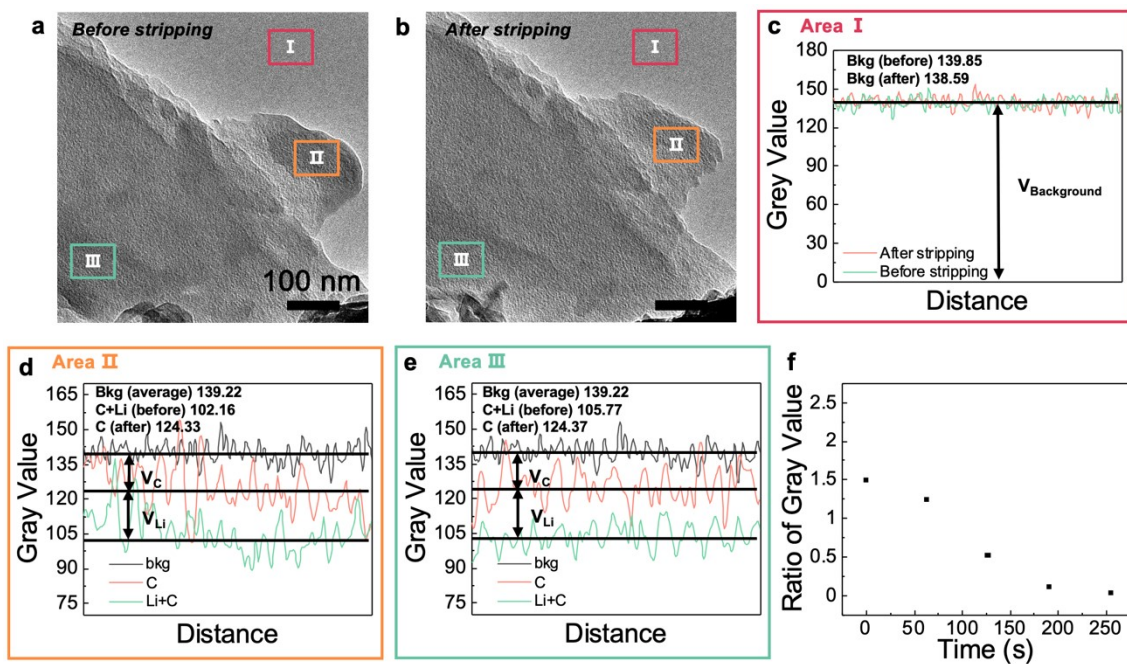
**Supplementary Fig. S14** | TEM images of graphite layers being annealed under (a) 300 °C and (b) 600 °C. When annealed at 300 °C, the interlayer structure is not sufficiently expanded and the ordered structure remains almost unchanged. When annealed at 600 °C, the graphite structure is largely etched into an amorphous structure, which can lower its electroconductivity. What is worse, the electrode would become fragile that can be easily pulverized. Hence, annealing at 450 °C delivers the most appropriate interlayer structure of BDLC.



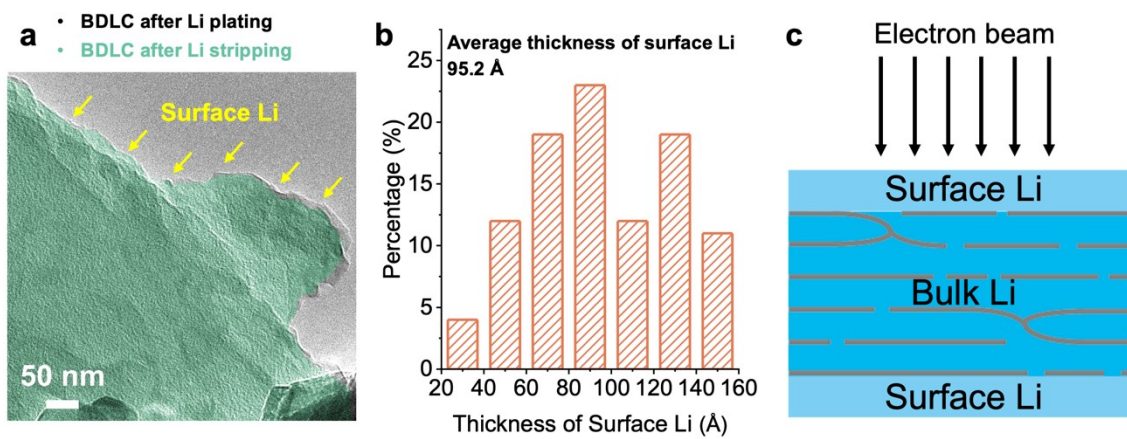
**Supplementary Fig. S15** | (a) SEM image of BDLC. (b) Scanning transmission electron microscopy image of BDLC and the corresponding EDS mapping images of C and N elements. (c) XPS survey, (d) C 1s and (e) N 1s spectra of BDLC. The C 1s spectrum can be deconvoluted into two sub-bands of C-C (284.127 eV) and C-N (285.95 eV). The N 1s spectrum demonstrates that the N active sites are composed of pyridinic N (399.04 eV), pyrrolic N (399.96 eV) and graphitic N (401.73 eV).



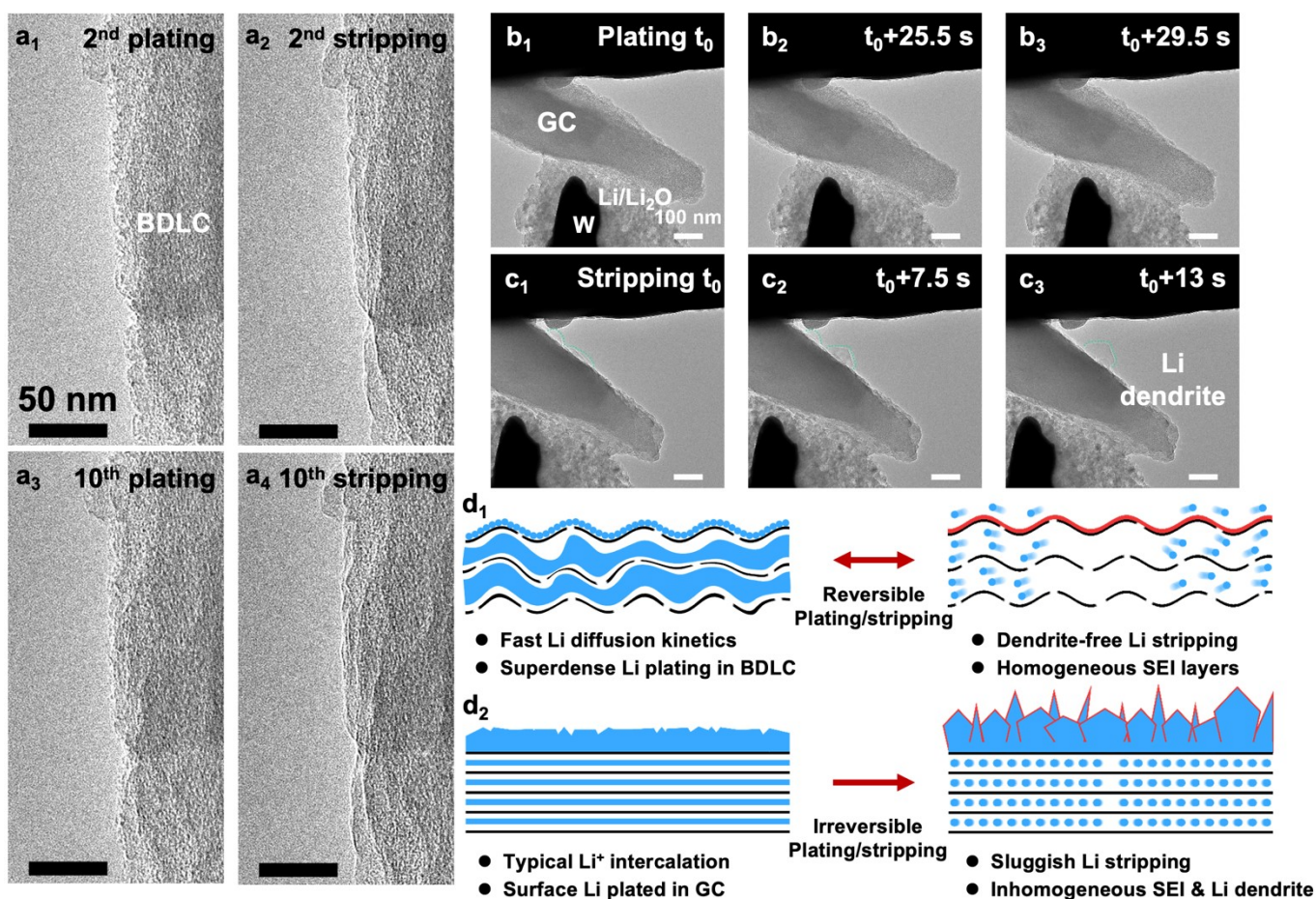
**Supplementary Fig. S16** | TEM images of (a) a nanosheet from BDLC placed between the Cu substrate and Li/Li<sub>2</sub>O solid electrolyte, (b) applied tension, (c) released tension. (d) Optical image of the bent BDLC. BDLC shows a good structural flexibility when the tension was applied or released from both microscopic and macroscopic conditions.



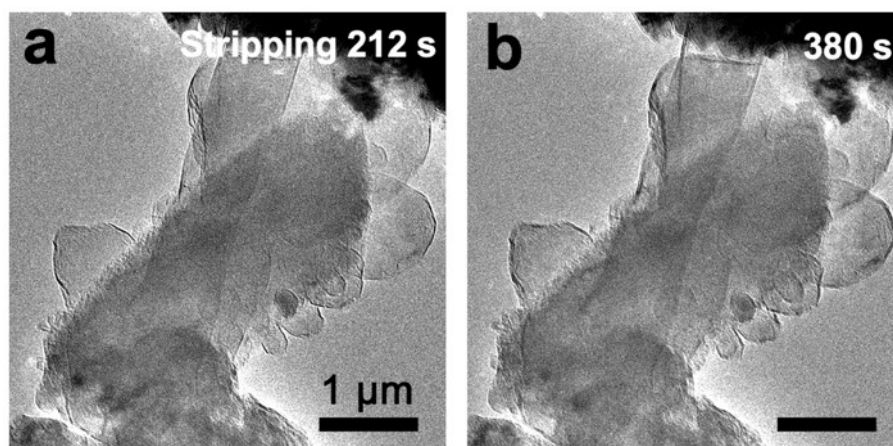
**Supplementary Fig. S17** | TEM images of BDLC (a) before and (b) after plating. The gray value distribution of (c) bkg before and after stripping, (d) C, C+Li, and bkg in Area II, and (e) C, C+Li, and bkg in Area III. (f) Change of Li/C gray value ratio over time. The gray value was measured by Image J.



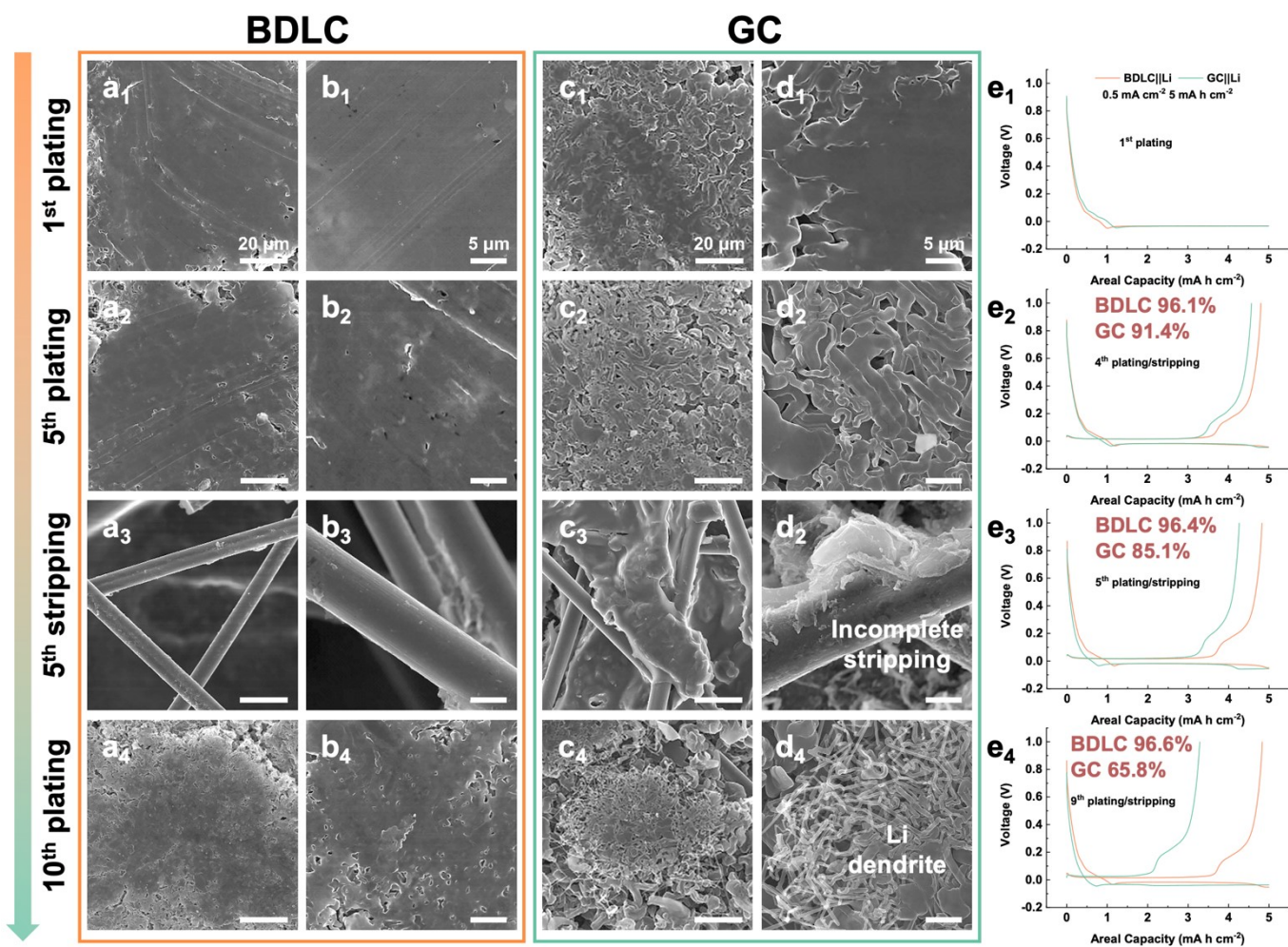
**Supplementary Fig. S18** | (a) In-situ TEM image of BDLC after Li plating (C+Li) with the overlapped area (light green) of BDLC after Li stripping (C). The surface Li can be distinguished for the measurement of thickness. (b) Statistics of thickness distribution of surface Li of BDLC, according to which the average thickness of surface Li is 95.2 Å. (c) Schematic illustration of an ideal Li deposition on the both sides of BDLC, considering the TEM imaging mode of transmission electrons.



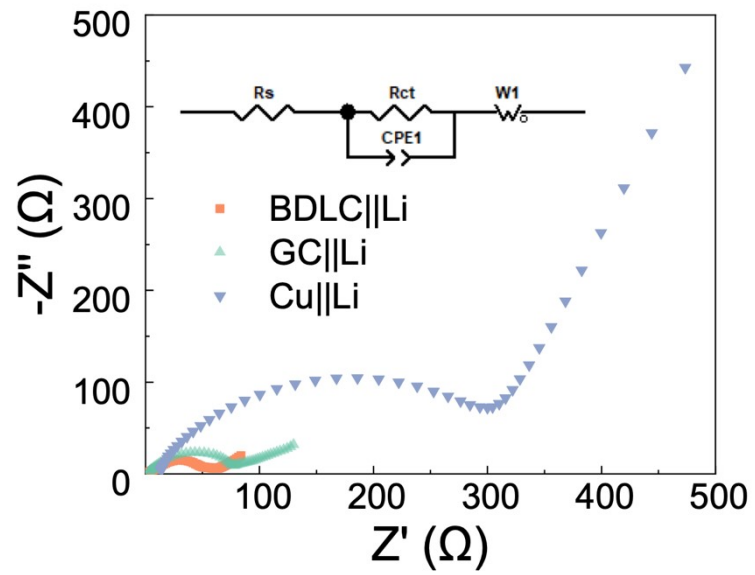
**Supplementary Fig. S19** | (a<sub>1</sub>-a<sub>4</sub>) In-situ TEM images of the 2<sup>nd</sup> and the 10<sup>th</sup> plating/stripping of BDLC selected from a 10 cycles reversible Li plating/stripping process under a higher magnification. (b<sub>1</sub>-b<sub>3</sub>, c<sub>1</sub>-c<sub>3</sub>) In-situ TEM images of an irreversible Li plating/stripping process of GC under a higher magnification. The growth of Li dendrite on the surface of GC are outlined with green dashed lines. (d) Comparative schematic illustration of Li plating/stripping between (d<sub>1</sub>) BDLC and (d<sub>2</sub>) GC according to in-situ TEM studies. In BDLC, multi-layered Li would be plated within the distorted and expanded atomic channels, and it can be reversibly plated/stripped with a fast Li diffusion kinetics. After a dendrite-free stripping of Li, a thin and homogeneous SEI layers would form. In comparison, Li would be plated on the surface of GC, and the sluggish Li diffusion commonly results in an inhomogeneous SEI and direct growth of Li dendrite.



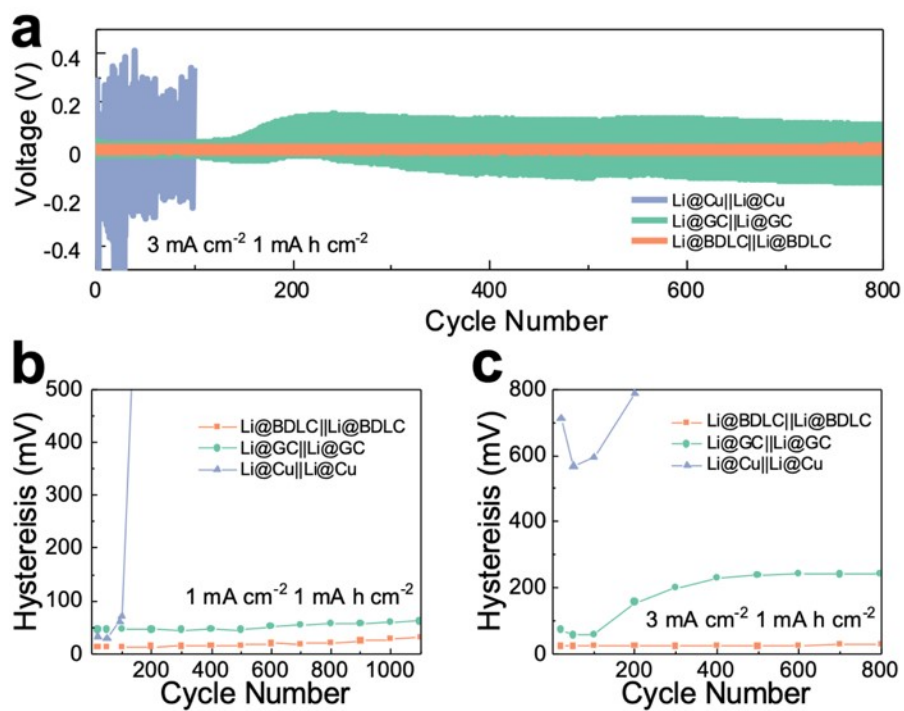
**Supplementary Fig. S20** | TEM images of GC stripped for (a) 212 s and (b) 380 s. The stripped Li becomes Li dendrite or dead Li that cannot be used in the following Li plating/stripping.



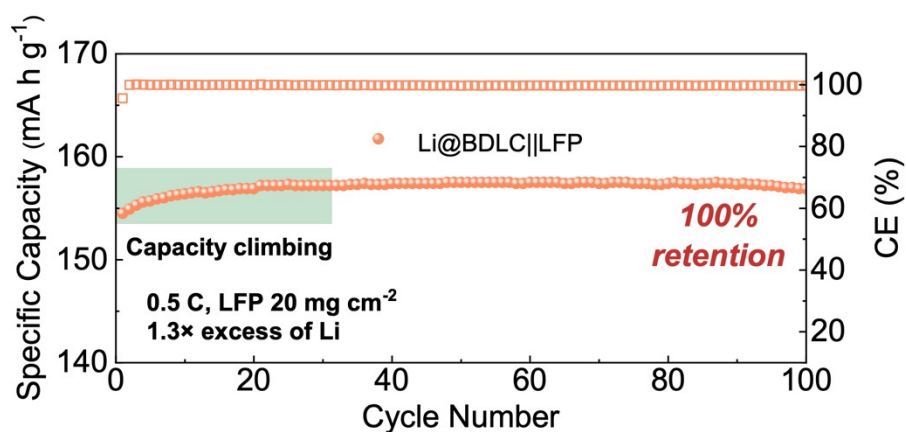
**Supplementary Fig. S21** | Ex-situ SEM characterization of Li plating/stripping morphologies at  $0.5 \text{ mA cm}^{-2}$  for  $5 \text{ mAh cm}^{-2}$  (after a pre-cycle at  $0.2 \text{ mA cm}^{-2}$  between 0 and 1.0 V for 5 cycles) at the 1<sup>st</sup>, 5<sup>th</sup> and 10<sup>th</sup> cycles, between BDLC ( $a_1$ - $a_4$ ,  $b_1$ - $b_4$ ) and GC ( $c_1$ - $c_4$ ,  $d_1$ - $d_4$ ). ( $e_1$ - $e_4$ ) The corresponding plating/stripping profiles of BDLC and GC.



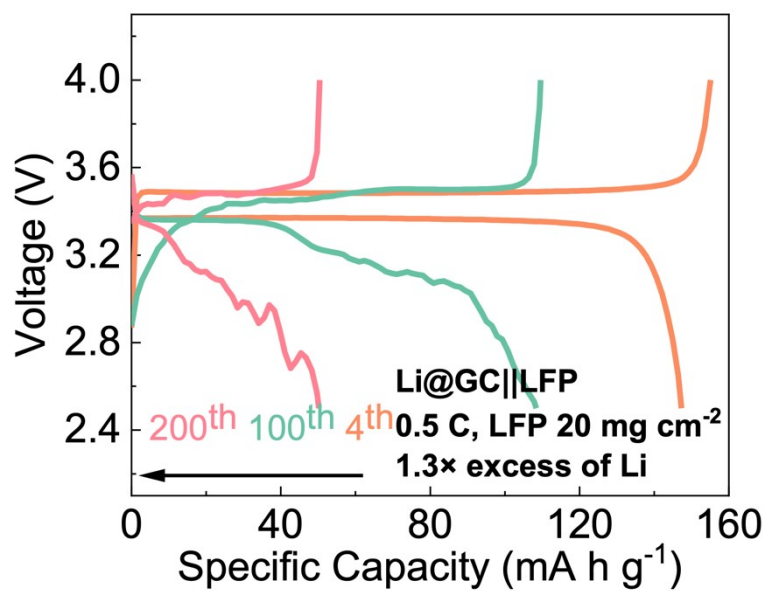
**Supplementary Fig. S22** | Nyquist curves of BDLC||Li, GC||Li and Cu||Li after 5 cycles under the current density of  $1 \text{ mA cm}^{-2}$  for  $2 \text{ mA h cm}^{-2}$ .



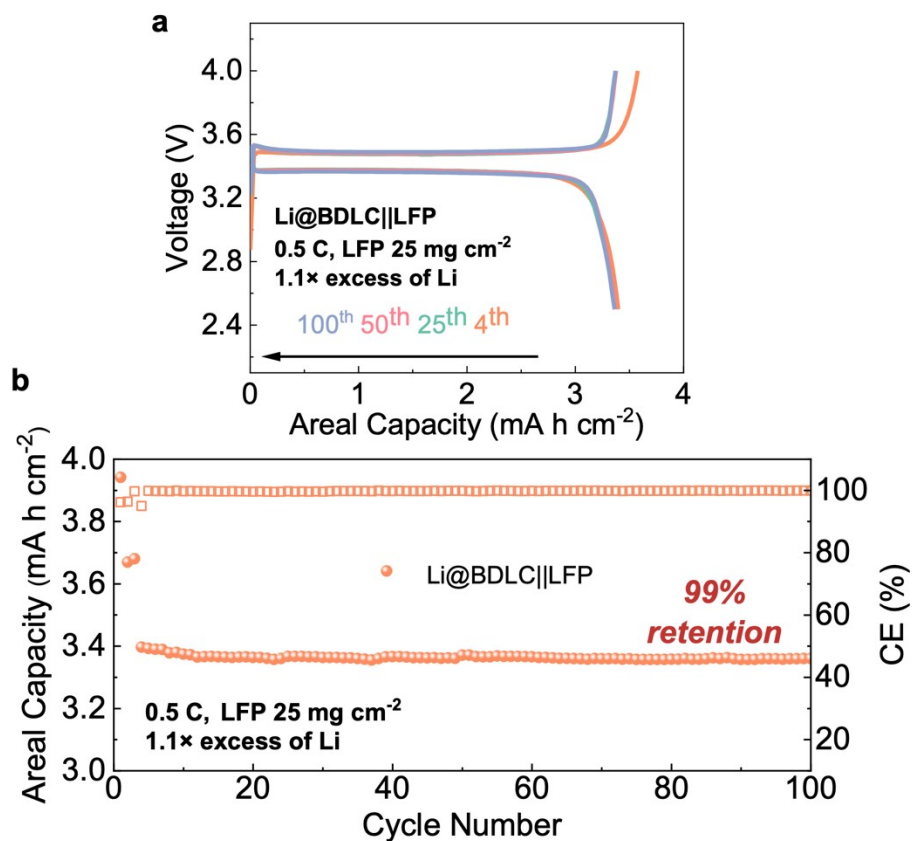
**Supplementary Fig. S23** | Constant charging/discharging voltage profiles of symmetric cells under the current density of 3 mA cm<sup>-2</sup> for 1 mA h cm<sup>-2</sup>. Plots of hysteresis symmetric cells under (b) 1 mA cm<sup>-2</sup>, 1 mA h cm<sup>-2</sup> and (c) 3 mA cm<sup>-2</sup>, 1 mA h cm<sup>-2</sup>.



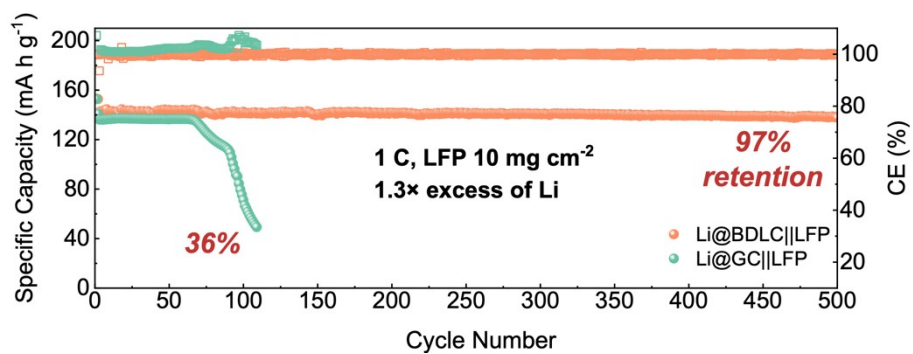
**Supplementary Fig. S24** | Cycling performance of Li@BDLC||LFP without battery activation at 0.5 C for three cycles (LFP 20 mg cm<sup>-2</sup>, 0.5 C, 1.3× excess of Li). Due to the high areal loading of LFP, it would take a longer time for battery activation, and cycling at a low rate for a few cycles is commonly adopted in most reported full-cell tests. As shown in Fig. S24, Li@BDLC||LFP would experience a capacity climbing over the initial 20 cycles. Therefore, in order to better take the advantage of LFP capacity, the full cells are activated for a few cycles between 2.5 and 4.0 V, for instance, 0.2 C for cycling performance and 0.05 C for rate performance.



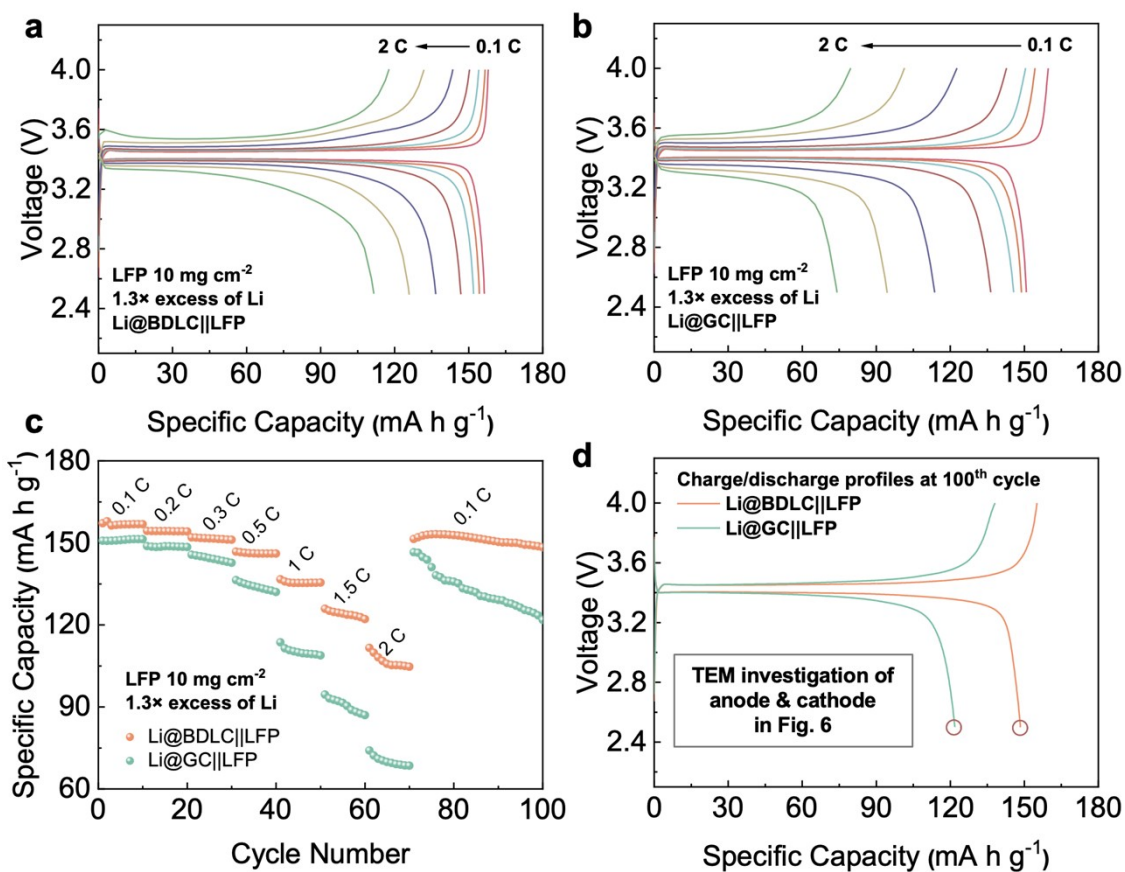
**Supplementary Fig. S25** | Charge/discharge profiles of Li@GC||LFP at the 4<sup>th</sup>, 100<sup>th</sup> and 200<sup>th</sup> corresponding to Figure 5e (LFP 20 mg cm<sup>-2</sup>, 1.3× excess of Li, 0.5 C).



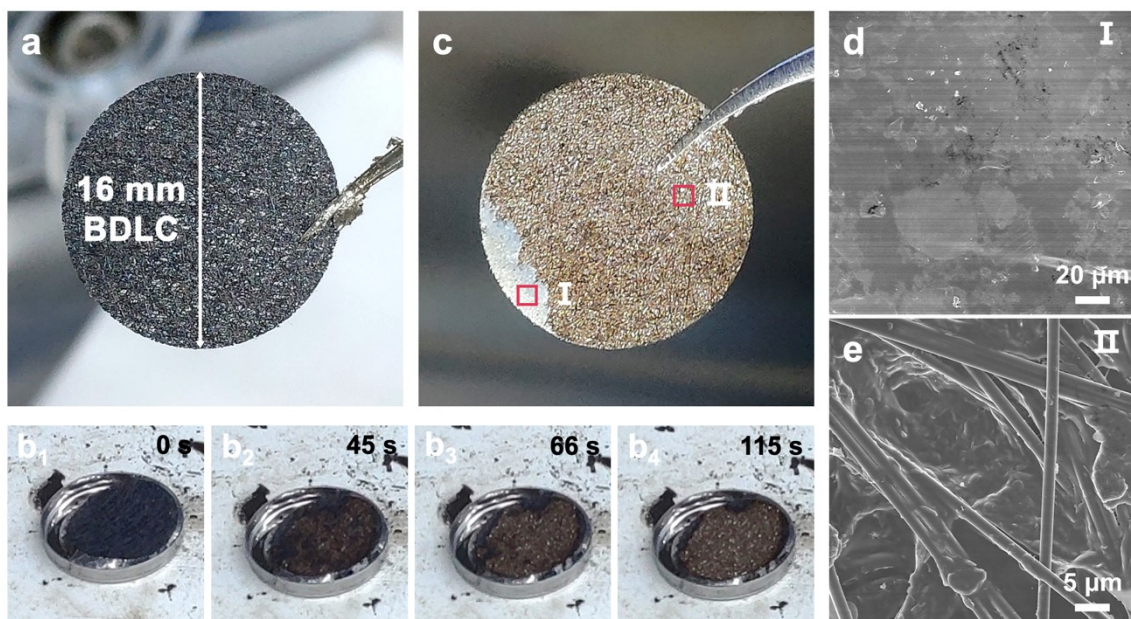
**Supplementary Fig. S26** | (1) Charge/discharge profiles of LFP cathode against Li@BDLC at the 4<sup>th</sup>, 25<sup>th</sup>, 50<sup>th</sup> and 200<sup>th</sup> with LFP areal loading of 25 mg cm<sup>-2</sup> at 2.07 mA cm<sup>-2</sup>. (a) Cycling performance of Li@BDLC||LFP with LFP areal loading of 25 mg cm<sup>-2</sup> at 2.07 mA cm<sup>-2</sup>.



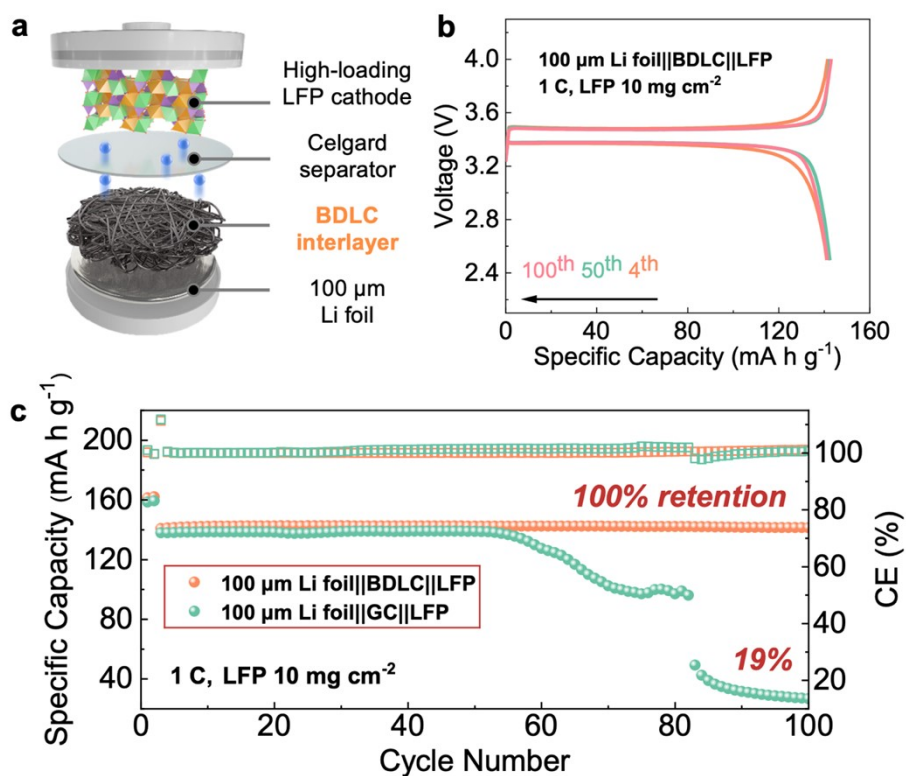
**Supplementary Fig. S27** | Comparison of cycling performance between Li@BDLC||LFP and Li@GC||LFP with LFP areal loading of 10 mg cm<sup>-2</sup> at 1 C (1.3× excess of Li).



**Supplementary Fig. S28** | (a, b) Charge/discharge profiles of Li@BDLC||LFP and Li@GC||LFP at various rates (LFP 10 mg cm<sup>-2</sup>, 1.3× excess of Li). (c) Rate capabilities of Li@BDLC||LFP and Li@GC||LFP at 0.1, 0.2, 0.3, 0.5, 1, 1.5 and 2 C (LFP 10 mg cm<sup>-2</sup>, 1.3× excess of Li). (d) Charge/discharge profiles of Li@BDLC||LFP and Li@GC||LFP at 100<sup>th</sup> cycle of rate performance.



**Supplementary Fig. S29** | Investigation of large-scale fabrication for practical application: molten Li adsorption to prepare Li@BDLC. (a) Optical photograph of pristine BDLC (16 mm in diameter). (b<sub>1</sub>-b<sub>4</sub>) Time series optical photographs during molten Li continuously adsorbed into BDLC. (c) Optical photograph of Li@BDLC after molten Li adsorption. (d-I, e-II) SEM images of Li@BDLC prepared by molten Li adsorption at specific areas.



**Supplementary Fig. S30** | Investigation of large-scale fabrication for practical application: using BDLC as an interlayer without pre-electrodeposition. (a) Schematic illustration of coin-type cell configuration, composed of high-loading LFP cathode (10 mg cm<sup>-2</sup>, 12 mm in diameter), Celgard separator, BDLC interlayer (16 mm in diameter) and 100 μm Li foil. (b) Charge/discharge profiles of 100 μm Li foil||BDLC||LFP at the 4<sup>th</sup>, 50<sup>th</sup> and 100<sup>th</sup> (LFP 10 mg cm<sup>-2</sup>, 1 C, without pre-electrodeposited Li). (c) Comparison of cycling performance between 100 μm Li foil||BDLC||LFP and 100 μm Li foil||GC||LFP over 100 cycles (LFP 10 mg cm<sup>-2</sup>, 1 C, without pre-electrodeposited Li).

### Section 3: Supplementary Tables S1-S4

**Supplementary Table S1** | The average charge and binding energy of different constructed sites.

	Average Charge	Binding Energy
Graphitic N	-1.17065	-1.07572
Pyridinic N <sub>SA</sub>	-1.16704	-5.35576
Pyridinic N <sub>DA</sub>	-1.11666	-4.73138
Pyrrolic N	-0.84601	-5.95083
Graphitic C	-0.10293	-0.95032
C <sub>SA</sub>	-0.08977	-2.53802
C <sub>DA</sub>	-0.21299	-2.79092
C <sub>TA</sub>	-0.23240	-3.10815

**Supplementary Table S2** | The comparison of the half-cell performance of our work with previously reported works.

Current Collector	Current Density (mA cm <sup>-2</sup> )	Capacity (mA h cm <sup>-2</sup> )	Cycle Number	CE
BDLC	1	2	200	98.30%
GC <sup>9</sup>	0.5	10	100	99%
Ag@GC <sup>10</sup>	-	-	-	(Ether-based electrolyte)
Ni@CC <sup>11</sup>	0.5	1	200	98.5
Nitrogen-doped carbon/ZnO <sup>12</sup>	1	1	200	(Ether-based electrolyte)
97.30%				
Porous dealloyed Cu <sup>13</sup>	1	1	120	97%
3D Cu <sub>2</sub> S NWs/Cu <sup>14</sup>	1	2	150	95.50%
Co <sub>3</sub> N/NF <sup>15</sup>	0.5	1	200	98.3%
TiO <sub>2</sub> nanotube arrays <sup>16</sup>	-	-	-	(Ether-based electrolyte)
-				
CuNW-P <sup>17</sup>	1	1	150	97.4%
Dynamic intelligent Cu <sup>18</sup>	1	1	800	(Ether-based electrolyte)
higher than 99%				
CuO@Cu foam <sup>19</sup>	1	1	270	97.10%
3DP Cu mesh <sup>20</sup>	1	5	500	95.50%
CuO NAs/CF <sup>21</sup>	1	5	100	98%
Ag/Cu <sup>22</sup>	1	1	100	94.50%
3D porous Cu-Zn alloy <sup>23</sup>	1	1	160	98.30%
Cu-Zn alloy <sup>24</sup>	1	1	200	97.90%
Graphene@Cu <sup>25</sup>	2	1	unmentioned	98%
rGO@Ni <sup>26</sup>	0.25	1	100	higher than 97%
CuNW <sup>27</sup>	1	3	120	about 97%

**Supplementary Table S3** | The  $R_{ct}$  and  $R_s$  table of BDLC, GC, and Cu.

	BDLC	GC	Cu
$R_{ct}$	53.84 $\Omega$	86.25 $\Omega$	337.9 $\Omega$
$R_s$	4.474 $\Omega$	2.12 $\Omega$	9.807 $\Omega$

**Supplementary Table S4** | The comparison of the full-cell performance of our work with previously reported works.

Current Collector	Cycle Rate (C)	Cycle Number	Retention Rate (against LFP)
BDLC	1	500	83.20%
GC <sup>9</sup>	4	600	76.30%
Ag@GC <sup>10</sup>	1	500	63%
Ni@CC <sup>11</sup>	0.5	330	91.70%
Nitrogen-doped carbon/ZnO <sup>12</sup>	2	200	unmentioned
Porous dealloyed Cu <sup>13</sup>	0.5	150	80%
3D Cu <sub>2</sub> S NWs/Cu <sup>14</sup>	0.5	100	95.50%
Co <sub>3</sub> N/NF <sup>15</sup>	0.5	600	93%
TiO <sub>2</sub> nanotube arrays <sup>16</sup>	1	400	54.80%
CuNW-P <sup>17</sup>	0.5	300	about 61.2%
Dynamic intelligent Cu <sup>18</sup>	unmentioned	500	89.10%
CuO@Cu foam <sup>19</sup>	1	100	80
3DP Cu mesh <sup>20</sup>	-	-	-
CuO NAs/CF <sup>21</sup>	0.2	250	90%
Ag/Cu <sup>22</sup>	1	200	unmentioned
3D porous Cu-Zn alloy <sup>23</sup>	-	-	-
Cu-Zn alloy <sup>24</sup>	1	400	unmentioned
Graphene@Cu <sup>25</sup>	0.5	100	98%
rGO@Ni <sup>26</sup>	1	350	88.50%
CuNW <sup>27</sup>	1	300	71%

#### **Section 4: Supplementary Movies S1-S5**

**Movie S1 .mp4** | In-situ TEM observation of a full Li plating/stripping process in BDLC. The as-plated Li metal would not be fixed in specific sites, but present a liquid-like diffusibility in BDLC. Then, the deposited Li metal could be completely stripped through the atomic channels of BDLC, showing a dendrite-free and fast bulk diffusion behavior. (Displayed with a 40× speed of a real time process)

**Movie S2 .mp4** | In-situ TEM observation of a full Li plating/stripping process for 10 cycles in BDLC under a higher magnification. The atomic channels in BDLC reveal a high stability during the reversible Li plating/stripping. (Displayed with a 60× speed of a real time process)

**Movie S3 .mp4** | In-situ SAED observation of a Li plating process in BDLC following Movie S2. A reciprocal lattice rod, attributed to the (110) plane of Li metal, is observed in the in-situ SAED investigation of BDLC. (Displayed with a 30× speed of a real time process)

**Movie S4 .mp4** | In-situ TEM observation of a Li plating/stripping process in GC. During plating, carbon nanosheet surface becomes rough with the growth of numerous Li crystal. What is worse, when the stripping begins, explosive growth of Li dendrites takes place in almost every direction of the carbon nanosheet. (Displayed with a 30× speed of a real time process)

**Movie S5 .mp4** | In-situ TEM observation of a Li plating/stripping process in GC under a higher magnification. Observation under a higher magnification further verify the sluggish Li diffusion and rapid Li dendrite growth of GC. (Displayed with a 5× speed of a real time process)

## Section 5: References

1. Kresse, G. & Furthmüller, J. Efficient iterative schemes for ab initio total-energy calculations using a plane-wave basis set. *Phys. Rev. B* **54**, 11169-11186, (1996).
2. Perdew, J. P., Burke, K. & Ernzerhof, M. Generalized gradient approximation made simple. *Phys. Rev. Lett.* **77**, 3865-3868, (1996).
3. Henkelman, G., Uberuaga, B. P. & Jónsson, H. A climbing image nudged elastic band method for finding saddle points and minimum energy paths. *J. Chem. Phys.* **113**, 9901-9904, (2000).
4. Grimme, S., Antony, J., Ehrlich, S. & Krieg, H. A consistent and accurate ab initio parametrization of density functional dispersion correction (DFT-D) for the 94 elements H-Pu. *J. Chem. Phys.* **132**, 154104, (2010).
5. Hutter, J., Iannuzzi, M., Schiffmann, F. & VandeVondele, J. Cp2k: atomistic simulations of condensed matter systems. *WIREs Comput. Mol. Sci.* **4**, 15-25, (2014).
6. Jain, A. *et al.* Commentary: The Materials Project: A materials genome approach to accelerating materials innovation. *APL Mater.* **1**, 011002, (2013).
7. Tanuma, S., Powell, C. J. & Penn, D. R. Calculations of electron inelastic mean free paths. *Surf. Interface Anal.* **37**, 1-14, (2005).
8. Chen, W., Cannon, F. S. & Rangel-Mendez, J. R. Ammonia-tailoring of GAC to enhance perchlorate removal. I: Characterization of NH<sub>3</sub> thermally tailored GACs. *Carbon* **43**, 573-580, (2005).
9. Zhou, X. *et al.* Enabling lithium-metal anode encapsulated in a 3D carbon skeleton with a superior rate performance and capacity retention in full cells. *ACS Appl. Mater. Interfaces* **10**, 35296-35305, (2018).
10. Zhang, R. *et al.* Coralloid carbon fiber-based composite lithium anode for robust lithium metal batteries. *Joule* **2**, 764-777, (2018).
11. Feng, Y.-Q. *et al.* A super-lithiophilic nanocrystallization strategy for stable lithium metal anodes. *Nano Energy* **73**, (2020).
12. Zhou, Y. *et al.* A nitrogen-doped-carbon/ZnO modified Cu foam current collector for high-performance Li metal batteries. *J. Mater. Chem. A* **7**, 5712-5718, (2019).
13. Shi, Y. *et al.* A self-supported, three-dimensional porous copper film as a current collector for advanced lithium metal batteries. *J. Mater. Chem. A* **7**, 1092-1098, (2019).
14. Huang, Z. *et al.* Realizing stable lithium deposition by in situ grown Cu<sub>2</sub>S nanowires inside commercial Cu foam for lithium metal anodes. *J. Mater. Chem. A* **7**, 727-732, (2019).

15. Lei, M. *et al.* Highly lithiophilic cobalt nitride nanobrush as a stable host for high-performance lithium metal anodes. *ACS Appl. Mater. Interfaces* **11**, 30992-30998, (2019).
16. Tantratian, K. *et al.* Stable Li metal anode enabled by space confinement and uniform curvature through lithiophilic nanotube arrays. *Adv. Energy Mater.* **10**, 1902819, (2019).
17. Zhang, C. *et al.* A lightweight 3D Cu nanowire network with phosphidation gradient as current collector for high-density nucleation and stable deposition of lithium. *Adv. Mater.* **31**, 1904991, (2019).
18. Chen, J. *et al.* Dynamic intelligent Cu current collectors for ultrastable lithium metal anodes. *Nano Lett.* **20**, 3403-3410 (2020).
19. Jiang, Y. *et al.* In situ growth of CuO submicro-sheets on optimized Cu foam to induce uniform Li deposition and stripping for stable Li metal batteries. *Electrochim. Acta* **339**, 135941 (2020).
20. Lim, G. *et al.* Robust pure copper framework by extrusion 3D printing for advanced lithium metal anodes. *J. Mater. Chem. A* **8**, 9058-9067, (2020).
21. Wei, L. *et al.* MOF-derived lithiophilic CuO nanorod arrays for stable lithium metal anodes. *Nanoscale* **12**, 9416-9422, (2020).
22. Hou, Z. *et al.* Lithiophilic Ag nanoparticle layer on Cu current collector toward stable Li metal anode. *ACS Appl. Mater. Interfaces* **11**, 8148-8154, (2019).
23. Fan, H., Dong, Q., Gao, C., Hong, B. & Lai, Y. Powder-sintering derived 3D porous current collector for stable lithium metal anode. *Mater. Lett.* **234**, 69-73, (2019).
24. Zhao, H. *et al.* Compact 3D copper with uniform porous structure derived by electrochemical dealloying as dendrite-free lithium metal anode current collector. *Adv. Energy Mater.* **8**, 1800266, (2018).
25. Yang, G. *et al.* Graphene anchored on Cu foam as a lithiophilic 3D current collector for a stable and dendrite-free lithium metal anode. *J. Mater. Chem. A* **6**, 9899-9905, (2018).
26. Yan, H. *et al.* Hosting ultrahigh areal capacity and dendrite-free lithium via porous scaffold. *ACS Sustain. Chem. Eng.* **6**, 4776-4783, (2018).
27. Fu, A. *et al.* Lithiophilic and antioxidative copper current collectors for highly stable lithium metal batteries. *Adv. Funct. Mater.* **31**, 202009805 (2021).